Front. Phys.
https://doi.org/10.15302/frontphys.2027.055204

CN 11-5994/O4
ISSN 2095-0462

RESEARCH ARTICLE

Critical Behavior and Magnetic Anisotropy in Room-Temperature Itinerant Ferromagnet Mn_2Ga_5

Sana Zahra,[1,2,*] Mishaal Irfan,[3,*] Ying Zhang,[1,4,†] Min Ge,[5] Pengzhi Chen,[1,2] Haitian Zhao,[1,2] Xitong Xu,[1] Zhenyu Li,[3,‡] Lei Zhang,[1,§] and Zhe Qu[1,¶]

[1] *Anhui Key Laboratory of Low-Energy Quantum Materials and Devices, High Magnetic Field Laboratory (CHMFL), Hefei Institutes of Physical Science, Chinese Academy of Sciences, Hefei 230031, China*

[2] *Science Island Branch of Graduate School, University of Science and Technology of China, Hefei 230026, China*

[3] *State Key Laboratory of Precision and Intelligent Chemistry, University of Science and Technology of China, Hefei 230026, China*

[4] *School of Electronic Engineering, Huainan Normal University, Huainan 232038, China*

[5] *The Instruments Center for Physical Science, University of Science and Technology of China, Hefei 230026, China*

Received June 16, 2026; accepted November 23, 2026

The pursuit and exploration of above-room-temperature itinerant ferromagnetic materials are highly desirable for advanced spintronic applications. As a typical itinerant ferromagnet, Mn_2Ga_5 has emerged as a promising candidate for spintronic devices due to its substantial magnetocrystalline anisotropy (MAE) and high Curie temperature (T_C). However, the intrinsic nature of its magnetic interactions remains inadequately clarified, which severely hinders its practical application. In this work, we systematically investigate the magnetic characteristics of Mn_2Ga_5 single crystals. High-precision magnetization measurements identify a second-order ferromagnetic phase transition at $T_C \approx 447$ K. Critical exponents ($\beta = 0.303$, $\gamma = 1.181$, and $\delta = 4.875$) are precisely determined via multiple analytical techniques, including modified Arrott plots, Kouvel-Fisher analysis, critical isotherms, and universality scaling approaches. The extracted critical exponents are close to those of the three-dimensional (3D) Ising universality class, indicating an effective 3D-Ising-like critical regime, with possible influence from anisotropy-driven crossover toward XY-like behavior. Furthermore,renormalization-group analysis suggests that the spin interaction approximately follows $J(r) \sim r^{-4.91}$. Density functional theory (DFT) based first-principles calculations demonstrate a ferromagnetic ground state with a tendency toward spin canting, with the magnetization preferentially oriented within the *ab* plane. Further validation based on self-consistent renormalization (SCR) theory confirms Mn_2Ga_5 as an in-plane itinerant ferromagnet. A prominent MAE of $K_u = 1442.1$ kJ/m^3 is also identified through quantitative analysis. These findings elucidate the unconventional critical behavior of Mn_2Ga_5, providing a fertile foundation for the design and development of next-generation spintronic devices.

Keywords: Mn_2Ga_5 single crystal, itinerant ferromagnet, critical phenomena, magnetic anisotropy, first-principle calculation

Just Accepted

This is a “Just Accepted” manuscript, which has been examined by the peer-review process and has been accepted for publication. A “Just Accepted” manuscript is published online shortly after its acceptance, which is prior to technical editing and formatting and author proofing. Higher Education Press (HEP) provides “Just Accepted” as an optional and free service which allows authors to make their results available to the research community as soon as possible after acceptance. After a manuscript has been technically edited and formatted, it will be removed from the “Just Accepted” Web site and published as an Online First article. Please note that technical editing may introduce minor changes to the manuscript text and/or graphics which may affect the content, and all legal disclaimers that apply to the journal pertain. In no event shall HEP be held responsible for errors or consequences arising from the use of any information contained in these “Just Accepted” manuscripts. To cite this manuscript please use its Digital Object Identifier (DOI®), which is identical for all formats of publication.

* These authors contributed equally to this work.
† yingzhang@hmfl.ac.cn
‡ zyli@ustc.edu.cn
§ zhanglei@hmfl.ac.cn
¶ zhequ@hmfl.ac.cn

Critical Behavior and Magnetic Anisotropy in Room-Temperature Itinerant Ferromagnet Mn_2Ga_5

Sana Zahra,[1,2,*] Mishaal Irfan,[3,*] Ying Zhang,[1,4,†] Min Ge,[5] Pengzhi Chen,[1,2] Haitian Zhao,[1,2] Xitong Xu,[1] Zhenyu Li,[3,‡] Lei Zhang,[1,§] and Zhe Qu[1,¶]

[1] *Anhui Key Laboratory of Low-Energy Quantum Materials and Devices, High Magnetic Field Laboratory (CHMFL), Hefei Institutes of Physical Science, Chinese Academy of Sciences, Hefei 230031, China*

[2] *Science Island Branch of Graduate School, University of Science and Technology of China, Hefei 230026, China*

[3] *State Key Laboratory of Precision and Intelligent Chemistry, University of Science and Technology of China, Hefei 230026, China*

[4] *School of Electronic Engineering, Huainan Normal University, Huainan 232038, China*

[5] *The Instruments Center for Physical Science, University of Science and Technology of China, Hefei 230026, China*

The pursuit and exploration of above-room-temperature itinerant ferromagnetic materials are highly desirable for advanced spintronic applications. As a typical itinerant ferromagnet, Mn_2Ga_5 has emerged as a promising candidate for spintronic devices due to its substantial magnetocrystalline anisotropy (MAE) and high Curie temperature (T_C). However, the intrinsic nature of its magnetic interactions remains inadequately clarified, which severely hinders its practical application. In this work, we systematically investigate the magnetic characteristics of Mn_2Ga_5 single crystals. High-precision magnetization measurements identify a second-order ferromagnetic phase transition at $T_C \approx 447$ K. Critical exponents ($\beta = 0.303$, $\gamma = 1.181$, and $\delta = 4.875$) are precisely determined via multiple analytical techniques, including modified Arrott plots, Kouvel-Fisher analysis, critical isotherms, and universality scaling approaches. The extracted critical exponents are close to those of the three-dimensional (3D) Ising universality class, indicating an effective 3D-Ising-like critical regime, with possible influence from anisotropy-driven crossover toward XY-like behavior. Furthermore,renormalization-group analysis suggests that the spin interaction approximately follows $J(r) \sim r^{-4.91}$. Density functional theory (DFT) based first-principles calculations demonstrate a ferromagnetic ground state with a tendency toward spin canting, with the magnetization preferentially oriented within the *ab* plane. Further validation based on self-consistent renormalization (SCR) theory confirms Mn_2Ga_5 as an in-plane itinerant ferromagnet. A prominent MAE of $K_u = 1442.1$ kJ/m^3 is also identified through quantitative analysis. These findings elucidate the unconventional critical behavior of Mn_2Ga_5, providing a fertile foundation for the design and development of next-generation spintronic devices.

Key words: Mn_2Ga_5 single crystal, itinerant ferromagnet, critical phenomena, magnetic anisotropy, first-principle calculation

I. INTRODUCTION

The binary Manganese Gallium (Mn-Ga) system has garnered significant interest in condensed matter physics due to its unique electromagnetic properties, including prominent magnetocrystalline anisotropy (MAE), metallic conductivity, and room-temperature ferromagnetism [1–7]. These superior characteristics position Mn-Ga based materials at the forefront of applications in topological spintronics [1, 8–10], permanent magnets [11], and magnetic memory [12, 13]. Among these materials, Mn_2Ga_5 receives particular attention as the only thermodynamically stable itinerant ferromagnet on the Ga-rich side, featuring a high Curie temperature ($T_C \approx 450$ K) and pronounced magnetic anisotropy [2, 14, 15]. It crystallizes in a tetragonal Mn_2Hg_5-type structure [16], which is topologically analogous to the Shastry-Sutherland lattice, forming a pattern of triangles and squares when viewed along the *c*-axis. This exotic structure hosts anisotropic Mn-Ga coordination, leading to a quasi-two-dimensional super-degenerate manifold of Mn $3d_{xz}$ and $3d_{yz}$ bands crossing the Fermi level. The resulting electronic structure generates itinerant ferromagnetism through an enhanced density of states (DOS) that satisfies the Stoner criterion [2]. Similar flat-band-enhanced magnetism and strong anisotropy have recently been observed in Ga-based itinerant magnets such as Fe_3GaTe_2 and FeGaTe [17].

In itinerant ferromagnets, magnetic ordering results from the collective alignment of spins in delocalized electrons through spin exchange interactions [18, 19]. These systems typically exhibit critical exponents conventionally close to those of mean-field or Heisenberg universality classes [20, 21], indicating long-range or short-range exchange interactions [22, 23]. However, this expectation becomes non-trivial in the presence of strong MAE. Generally, MAE reduces the effective symmetry of the in-

* These authors contributed equally to this work.
† yingzhang@hmfl.ac.cn
‡ zyli@ustc.edu.cn
§ zhanglei@hmfl.ac.cn
¶ zhequ@hmfl.ac.cn

teraction dimensionality and can significantly alter critical fluctuations near the critical temperature, potentially driving the system toward lower-symmetry and intermediate universality classes, such as the three-dimensional (3D) Ising or 3D-XY type [24, 25]. This raises a fundamental and still unresolved question for anisotropic itinerant ferromagnets: how does the competition between itinerant exchange and strong anisotropy influence their universality class and effective interaction range near T_C? Addressing this question not only involves determining critical exponents, but also tests the validity of Landau-Ginzburg theory in systems where competition exists between orbital hybridization, strong magnetic anisotropy, and itinerancy [26].

To address this question, we synthesized high-quality single crystal of Mn_2Ga_5 and thoroughly examined its magnetic critical behavior in the vicinity of T_C. Magnetization measurements reveal a second-order ferromagnetic (FM)-paramagnetic (PM) transition with significant magnetic anisotropy. Using a series of techniques, such as modified Arrott plots, Kouvel-Fisher analysis, and universality scaling, we extracted reliable critical exponents. These critical exponents are close to those of the 3D-Ising universality class, and the magnetic exchange interaction decaying as $J(r) \approx r^{-4.91}$. We confirmed the itinerancy of the Mn_2Ga_5 single crystal through Curie-Weiss analysis and the Rhodes-Wohlfarth ratio. In addition, we identified a significant MAE of $K_u = 1442.1$ kJ/m^3 as predicted by first-principles calculations using density functional theory (DFT). Our analysis further reveals a ground state with a possible non-collinear spin configuration, arising from a canted spin structure induced by competing exchange interactions among the Mn sublattices. By evaluating the total energy of various spin orientations, we established the easy magnetization plane within the *ab*-plane and the hard axis along the *c*-axis. Furthermore, SCR theory validates Mn_2Ga_5 as an in-plane itinerant ferromagnet. Our results establish Mn_2Ga_5 as an itinerant ferromagnet with pronounced easy-plane anisotropy. The extracted critical exponents suggest anisotropic 3D critical behavior, with possible crossover effects between Ising and XY-like universality regimes, and provide new insight into critical phenomena in anisotropic itinerant magnetic systems.

II. EXPERIMENTAL METHODS AND FIRST-PRINCIPLES CALCULATIONS

Single crystals of Mn_2Ga_5 were grown using a self-flux method [27]. High-purity dendritic Mn pieces and Ga shots, mixed in a molar ratio of 1 : 20 with gallium as an effective flux, served as the starting materials. The weighed materials were loaded into pre-baked fused silica tubes. To facilitate crystal separation from the residual flux, silica wool was placed at the bottom of the tube, with an additional layer above the charge. The tubes were evacuated to approximately 10^{-6} Torr and flame-sealed. All handling was performed in a nitrogen-filled glove box, maintained at an oxygen level of 0.1 ppm to minimize contamination and oxidation of the reactive elements. The sealed ampoules were placed vertically inside a programmable furnace and heated to 800 °C for 10 hours to ensure complete homogenization. The tubes were then allowed to cool to 500 °C, where they remained for three days. Subsequently, the ampoules were quickly removed from the furnace, inverted, and placed in a centrifuge to separate any residual Ga flux from the crystals.

The crystalline structure and phase purity of Mn_2Ga_5 were examined by X-ray diffraction (XRD) using a Rigaku TTR3 diffractometer with Cu Kα radiation. Rietveld refinement of the data was carried out using the GSAS-II software package to obtain lattice parameters. Chemical composition was verified by Energy Dispersive X-ray (EDX) Spectroscopy with an Oxford Instruments detector. To further investigate the crystal structure, high-angle annular dark-field scanning transmission electron microscopy (HAADF-STEM) was conducted using a Themis Z double-spherical aberration-corrected transmission electron microscope. The temperature, field, and angle dependence of magnetization were measured with a superconducting quantum interference device vibrating sample magnetometer (SQUID-VSM) (Quantum Design, MPMS-3). Isothermal magnetization curves were recorded over a temperature range of $437 - 457$ K, with 1 K intervals around T_C. A waiting period of 20 minutes was held before recording each isotherm to ensure temperature stabilization.

First-principles calculations were performed utilizing density functional theory (DFT) as implemented in the Vienna Ab initio Simulation Package (VASP) [28]. The structural model was constructed from the experimentally refined Mn_2Ga_5 crystal structure obtained through Rietveld refinement of our powder XRD data. The refined lattice parameters and atomic coordinates were directly used to build the computational model. The resulting structure adopts the tetragonal space group $P4/mbm$ (No. 127). The exchange-correlation potential was handled using the spin-polarized Local Density Approximation (LDA), while electron-ion interactions were treated by the Projector Augmented Wave (PAW) method [29]. LDA was chosen as it provides a reliable description of the Mn($3d$)-Ga($4p$) hybridization and magnetic properties of itinerant Mn_2Ga_5, while GGA, GGA+U, and LDA+U approaches can lead to an overestimation of lattice parameters and local Mn magnetic moments. All total energy calculations were performed using a plane-wave basis set with a kinetic energy cutoff of 520 eV. Structural relaxations, magnetic ground-state determination, and equation-of-state (EOS) volume-dependent energy calculations were carried out using a Γ-centered $6 \times 6 \times 12$ Monkhorst-Pack k-point mesh. Methfessel-Paxton smearing with a width of $\sigma = 0.05$ eV was employed to accurately treat the metallic electronic structure. The convergence criteria were maintained at 10^{-6} eV for total energy and 0.01 eV/Å for atomic forces dur-

ing structural optimization. The total energies of ferromagnetic and various antiferromagnetic configurations were compared to identify the magnetic ground state. To explore non-collinear magnetism, self-consistent calculations were performed both with and without spin-orbit coupling (SOC). Fully relativistic SOC calculations were carried out with stringent electronic convergence criteria of EDIFF = 10^{-7}-10^{-8} eV to accurately determine the non-collinear magnetic ground state and magnetocrystalline anisotropy energy (MAE). Considering the large tetragonal cell anisotropy ($c/a \approx 0.30$), an aspect-ratio-matched dense $8 \times 8 \times 24$ Monkhorst-Pack k-point mesh (1536 k-points in the full Brillouin zone, $\Delta k < 0.09$ Å^{-1}) was employed for all SOC calculations to ensure uniform Brillouin-zone sampling [30]. The magnetocrystalline anisotropy energy (ΔE_{MAE}) was determined from the self-consistent total energy differences with the spin quantization axis aligned along the hard [001] c-axis and the in-plane [100] and [110] easy axes. The angular dependence of the anisotropy energy was further mapped through constrained non-collinear total-energy calculations by rotating the magnetization direction over polar angles $\theta = 0°$-$180°$ with respect to the c-axis [30].

III. RESULTS AND DISCUSSION

Figure 1 (a) presents the [001] projection view (top) along the c-axis and unit cell crystal structure of Mn_2Ga_5 (bottom). Isostructural to the Mn_2Hg_5-type, Mn_2Ga_5 exhibits tetragonal symmetry with the space group $P4/mbm$ (No. 127) [16]. The structure consists of Mn atoms positioned within pentagonal prisms formed by two crystallographically distinct types of Ga atoms. Each pentagonal prism comprises 10 Ga atoms: two from Ga(1) and eight from Ga(2). These $MnGa_{10}$ prisms are stacked along the c-axis, with adjacent prisms sharing faces, creating a robust 3D network. As shown in Fig. 1 (a), the arrangement of Mn magnetic ions bears a superficial resemblance to a Shastry-Sutherland-like lattice, characterized by geometric configurations of triangles and squares [31, 32]. This configuration could lead to competing exchange interactions between nearest-neighbor Mn atoms (J_1) through Mn-Mn pathway and next-nearest-neighbor Mn atoms (J_2) via Mn-Ga-Mn exchange pathways. The Mn-Ga bond distances range from 2.611 Å to 2.738 Å, with Ga-Mn-Ga bond angles varying from 59.3° to 62.5° along the c-axis [2].

To investigate the atomic structure of Mn_2Ga_5, aberration-corrected HAADF-STEM imaging was performed, with the atomic-resolution image depicted in Fig. 1 (b). Analysis of the d-spacing corresponding to the (310) and (320) planes yields lattice parameters of $a = b = 8.85 \pm 0.01$ Å, consistent with previously reported values [2]. The right inset of Fig. 1 (b) shows the fast Fourier transform (FFT) pattern derived from the HAADF-STEM image, featuring sharp and well-defined diffraction spots, further confirming the high crystallinity of the sample. Figure 1 (c) presents the STEM-EDX elemental mapping of the Mn_2Ga_5 crystal, revealing a homogeneous distribution of Mn and Ga elements. Figure 1 (d) displays the Rietveld refinement profile of the powder XRD pattern for Mn_2Ga_5. The experimental diffraction pattern is well reproduced by the calculated profile, confirming that Mn_2Ga_5 crystallizes in a tetragonal $P4/mbm$ structure. The refined lattice parameters are $a = b = 8.851(4)$ Å and $c = 2.709(5)$ Å, which are in excellent agreement with previously reported values [2]. The refined crystallographic parameters and atomic coordinates are summarized in Tables S4 and S5 in the Supplementary Material [33]. The as-grown single crystals exhibit a needle-like morphology, as depicted in the inset of Fig. 1 (e). All observed diffraction peaks are well indexed and agree with the simulated Bragg reflections of Mn_2Ga_5 obtained from the Crystallography Open Database (COD-4107348) [11], as shown in Fig. S3. The sharp and well-resolved diffraction peaks confirm the high structural quality and phase purity of the as-grown crystals. To determine the chemical composition, energy-dispersive X-ray spectroscopy (EDX) measurements were performed at multiple locations across the single crystal surface. As shown in Fig. 1 (e), the analysis yields a stoichiometry of Mn : Ga = 2.00 : 4.96, closely approximating the desired ratio. All results, including HAADF-STEM, STEM-EDX, XRD, and EDX, demonstrate the excellent crystallinity and high quality of the as-grown Mn_2Ga_5 single crystals.

Figure 2 (a) displays the temperature-dependent magnetization [$M(T)$] of single-crystal Mn_2Ga_5 measured at $H = 1000$ Oe with the field applied parallel to both the ab-plane ($H \parallel ab$) and the c-axis ($H \parallel c$). The $M(T)$ curves are obtained in both zero-field-cooled (ZFC) and field-cooled (FC) modes. The Curie temperature $T_C \sim 447$ K is clearly identified by the derivative dM/dT [inset of Fig. 2 (a)], which is a hallmark of critical behavior near a phase transition. Upon cooling, the magnetization exhibits a sharp increase, characterized by an abrupt transition from a paramagnetic to a ferromagnetic state, with slight splitting between the ZFC and FC curves. Such bifurcation is commonly observed in ferromagnetic systems and is generally associated with irreversible domain processes influenced by magnetic anisotropy [34]. In Mn_2Ga_5, this weak ZFC-FC separation is attributed to anisotropy-driven domain dynamics during the magnetic ordering transition. The absence of pronounced ZFC-FC irreversibility suggests that Mn_2Ga_5 does not exhibit a spin-glass-like transition. However, weak macroscopic irreversibility does not exclude possible microscopic competition among exchange interactions that may influence the magnetic ground state. The magnetization values for $H \parallel ab$ are substantially larger than those for $H \parallel c$, identifying the ab-plane as the easy magnetization plane [35–37]. In materials with strong anisotropic properties, the orientation of the applied field significantly influences magnetic behavior [38]. Below T_C, the magnetization rapidly increases with decreasing temperature and satu-

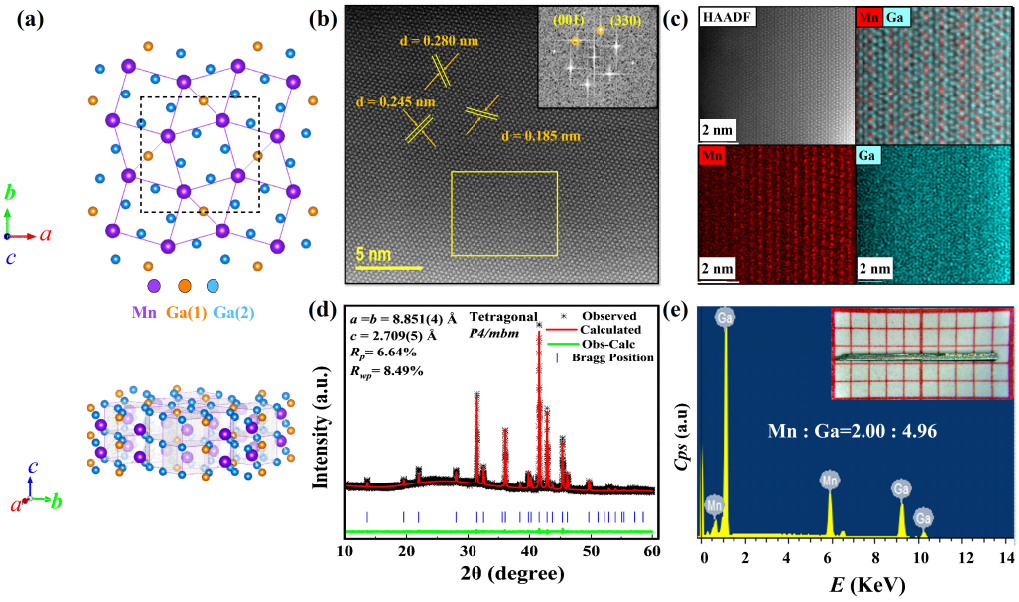


FIG. 1. (a) Top: Schematic crystal structure of Mn_2Ga_5 viewed along the [001] (c-axis) direction, showing the Shastry-Sutherland-like arrangement of Mn magnetic ions. Bottom: The unit-cell structure of Mn_2Ga_5, where purple, orange, and light-blue spheres represent Mn, Ga(1), and Ga(2) atoms, respectively. The crystallographic axes a, b, and c correspond to the [100], [010], and [001] directions, respectively. (b) HAADF-STEM image of Mn_2Ga_5 at atomic resolution. The right inset displays the corresponding Fast Fourier transform (FFT) diagram within the yellow rectangular region. (c) Elemental mapping of Mn_2Ga_5, obtained from HAADF-EDX spectroscopy. (d) Rietveld refinement of powder X-ray diffraction (XRD) pattern for Mn_2Ga_5 at room temperature. (e) Typical EDX spectrum of Mn_2Ga_5 single crystal with composition nearly equal to the stoichiometric ratio. Inset: Image of a representative as-grown single crystal of Mn_2Ga_5, with approximately 9 mm in length along the c-axis and 1 mm^2 in cross-sectional area.

rates at low temperatures, consistent with conventional ferromagnetic behavior. The saturation is more pronounced along the easy direction ($H \parallel ab$), further confirming the strong anisotropy of this material. The easy magnetization along the ab-plane suggests a quasi-2D nature of the Mn-sublattice, attributed to orbital interactions in the ab-plane as indicated by electronic structure calculations [2].

To elucidate the nature of magnetism in Mn_2Ga_5, we fitted the $M(T)$ curves above $T^* \sim 470$ K in both directions using the Curie-Weiss law $\chi = C/(T - \Theta_{CW})$, where Θ_{CW} is the Curie-Weiss temperature and C is the Curie constant. For $H \parallel ab$, the linear fit of the inverse susceptibility $\chi^{-1}(T)$ in the paramagnetic region yields $\Theta^{ab}_{CW} = 462.5$ K with $\mu^{ab}_{eff} = 5.50\ \mu_B$/f.u. In contrast, for $H \parallel c$, the corresponding fit gives $\Theta^{c}_{CW} = 450.0$ K with $\mu^{c}_{eff} = 4.16\ \mu_B$/f.u., as shown in Fig. 2 (b). The reliability of the Curie-Weiss fitting was evaluated using the coefficient of determination (R^2), with values higher than 0.996 for both $H \parallel ab$ and $H \parallel c$, confirming excellent linear fitting behavior in the paramagnetic region. The positive Θ_{CW} values for both directions indicate dominant ferromagnetic exchange interactions in Mn_2Ga_5. The effective moments obtained from the Curie-Weiss fits are smaller than the spin-only value of $g\sqrt{S(S+1)} = 5.92\ \mu_B$ expected for high-spin Mn^{2+} with $S = 5/2$. This reduction suggests the presence of itinerant electronic contributions arising from Mn-Ga hybridization and partial electron delocalization. However, the reduced Curie-Weiss effective moment alone cannot be considered as definitive evidence of itinerant magnetism, as the measured moments can also be affected by exchange interactions, spin fluctuations, and deviations from the ideal ionic Mn^{2+} state. Therefore, the itinerant character was further evaluated using the Rhodes-Wohlfarth ratio (RWR).

The well-known RWR, defined as $R = q_c/q_s$, is an established criterion for distinguishing between localized and itinerant magnetic moments in a system [39]. Here, q_c relates to the effective moment, with the equation $q_c(q_c + 2) = \mu^2_{eff}$. Given that Mn_2Ga_5 contains two Mn atoms per formula unit, the magnetic moments were normalized per Mn atom for the calculation. A system is considered to have localized moments when $R \sim 1$, while itinerant moment systems have $R \gg 1$. For Mn_2Ga_5, we find $R^{ab} = 2.22$ for $H \parallel ab$ and $R^{c} = 1.55$ for $H \parallel c$, respectively, as detailed in Table I. Both ratios exceed unity, indicating a deviation from localized moments and suggesting the presence of itinerant magnetic contributions in Mn_2Ga_5. The larger Θ^{ab}_{CW} and μ^{ab}_{eff} values suggest stronger magnetic interactions and enhanced spin correlations within the easy magnetization plane, where exchange interactions are more robust. The anisotropy observed in RWR reflects anisotropic exchange inter-

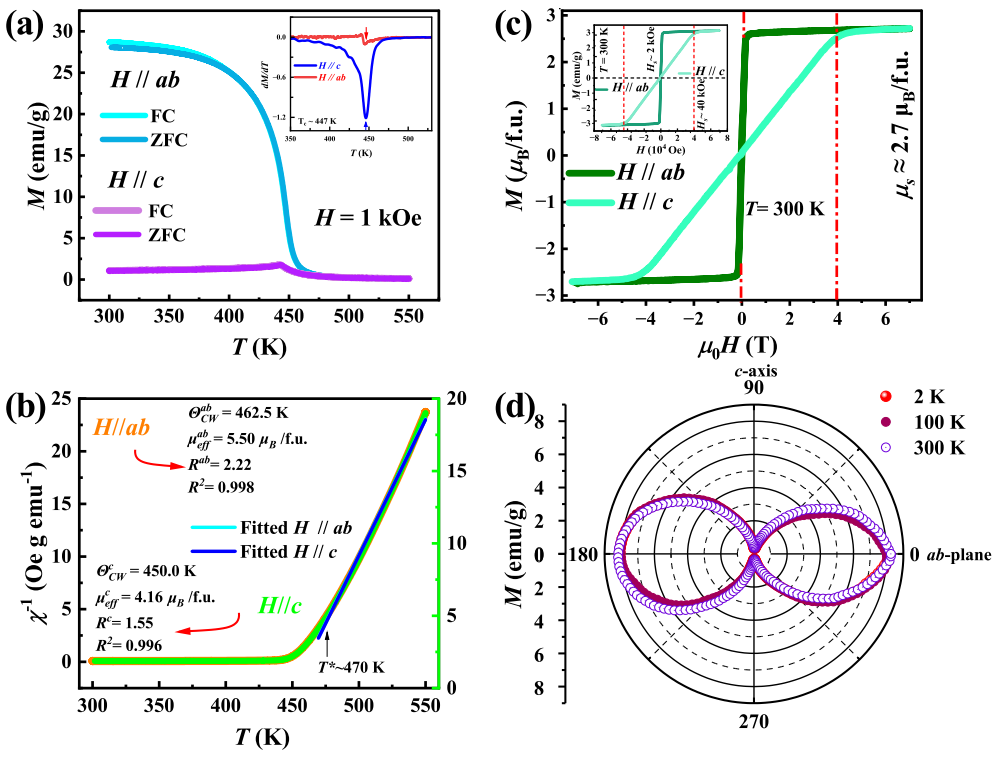


FIG. 2. (a) Temperature-dependent magnetization $[M(T)]$ of Mn_2Ga_5 single crystal under $H = 1$ kOe, with the field applied along the ab-plane and c-axis. Inset: dM/dT vs. T. (b) The reciprocal of susceptibility $[\chi^{-1}(T)]$ for $H \parallel ab$ and $H \parallel c$ directions, fitted by the Curie-Weiss law represented by blue lines. (c) Field-dependent magnetization $[M(H)]$ of Mn_2Ga_5 measured at $T = 300$ K. (d) Angle-dependent magnetization $[M(\varphi)]$ at $T = 2$ K, 100 K, and 300 K under $H = 1$ kOe.

TABLE I. Curie-Weiss temperatures ($\Theta_{\rm CW}$), effective moments ($\mu_{\rm eff}$), saturation moments (μ_S), and Rhodes-Wohlfarth parameters of Mn_2Ga_5 single crystal. The effective and saturation moments are listed per formula units. The Rhodes-Wohlfarth parameters are evaluated per Mn atom using $\mu_{\rm eff}({\rm Mn}) = \mu_{\rm eff}({\rm f.u.})/\sqrt{2}$ and $q_s = \mu_s({\rm f.u.})/2$.

Axis	$\Theta_{\rm CW}$ (K)	$\mu_{\rm eff}$ (μ_B/f.u.)	$\mu_{\rm eff}$ (μ_B/Mn)	μ_s (μ_B/f.u.)	q_c	q_s	q_c/q_s
$H \parallel ab$	462.5	5.50	3.89	2.71	3.02	1.355	2.22
$H \parallel c$	450.0	4.16	2.94	2.72	2.11	1.36	1.55

actions, consistent with the predicted superdegenerate band topology in the ab-plane.

Figure 2 (c) presents the field-dependent magnetization $[M(H)]$ at $T = 300$ K up to 7 T for both $H \parallel ab$ and $H \parallel c$ directions. For $H \parallel ab$, the magnetization saturates rapidly at $\mu_S^{ab} \approx 2.71$ μ_B/f.u. (33 emu/g) with a saturation field of $H_S \approx 2$ kOe. In contrast, for $H \parallel c$, the magnetization increases more gradually, reaching saturation at $\mu_S^c \approx 2.72$ μ_B/f.u. (33.15 emu/g) with a much higher $H_S \approx 40$ kOe. The saturated moments obtained from both directions closely match the value reported by Kim *et al.* [2]. The lower H_S along the ab-plane confirms that the ab-plane is the easy magnetization plane. The difference in the approach to saturation in the $M(H)$ curves between the different directions supports the presence of strong anisotropic MAE in Mn_2Ga_5. To verify this, we performed the angular dependence of magnetization $[M(\varphi)]$ at $T = 2$, 100, and 300 K under $H = 1000$ Oe, as shown in Fig. 2 (d). We observed the complete magnetic evolution process between both directions by rotating the magnetic field from the ab-plane to the c-axis [33]. The $[M(\varphi)]$ data clearly reveal a characteristic dumbbell-shaped pattern with two-fold symmetry, showing maxima at $\varphi = 0°$ and 180° ($H \parallel ab$) and minima at $\varphi = 90°$ and 270° ($H \parallel c$). This 180° periodicity provides unambiguous evidence for MAE, with the ab-plane as the easy plane and the c-axis as the hard axis. These findings are fully consistent with the experimental $M(H)$ and $M(T)$ curves, confirming itinerant ferromagnetism with strong anisotropy in Mn_2Ga_5.

We performed DFT calculations to determine the magnetic ground state structure of Mn_2Ga_5. Initially, we ex-

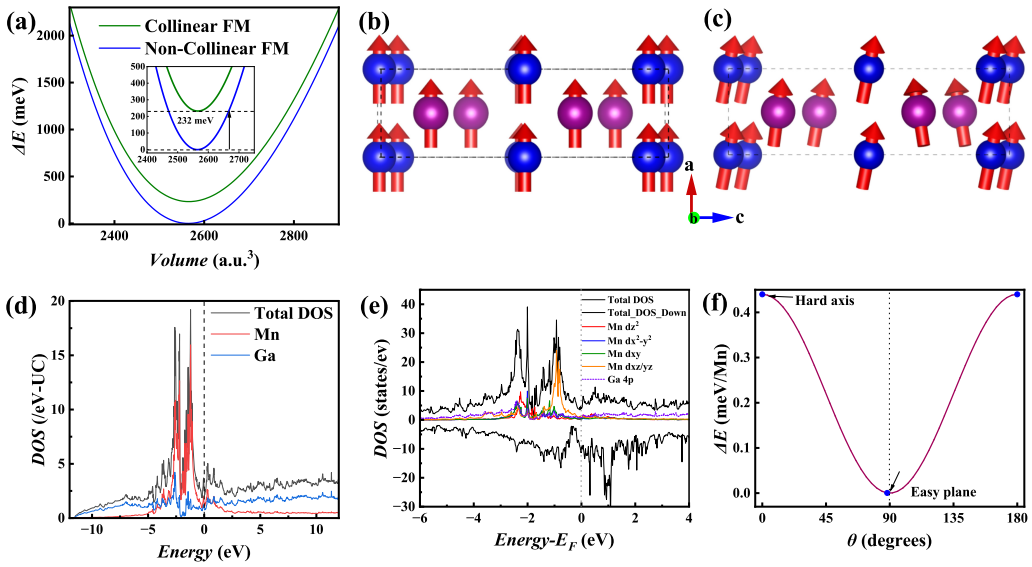


FIG. 3. (a) Total energy (ΔE) as a function of unit cell volume for the collinear (green) and non-collinear (blue) ferromagnetic states. Inset: The non-collinear ground state is stabilized by 232 meV relative to the collinear phase. (b) Schematic spin-textures of the collinear ferromagnetic and (c) non-collinear ferromagnetic configurations. (d) Spin-polarized total and site-projected density of states (PDOS). The dashed vertical line represents the Fermi level ($E_F = 0$ eV). The total DOS (black line) exhibits significant exchange splitting, with the Mn-3d partial DOS (red) dominating the electronic structure near E_F. The Ga-projected DOS (blue) remains relatively featureless across the valence region. (e) Spin-polarized total and orbital-projected density of states (PDOS) for Mn_2Ga_5. The Fermi level (E_F) is referenced at 0 eV (vertical dashed line). The spin-up majority manifold shows prominent Mn-3d states (d_{z^2}, $d_{x^2-y^2}$, d_{xy}, and degenerate d_{xz}/d_{yz}) hybridizing with delocalized Ga-4p states across the energy range from -4.0 eV to 0 eV. In contrast, the spin-down minority Mn-3d states remain unoccupied and positioned predominantly above the Fermi level (+0.2 eV to +2.0 eV). (f) Evolution of the total energy (ΔE) as a function of the spin orientation angle (θ) relative to the c-axis.

TABLE II. Relative energies ΔE (eV/f.u.) and average magnetic moments M (μ_B) on Mn and Ga atoms for different spin configurations of Mn_2Ga_5 calculated by PAW method.

Magnetic state	ΔE (eV/f.u.)	M_{Mn} (μ_B)	M_{Ga} (μ_B)
Non-magnetic	0	0	0
FM	−0.609	2.14	−0.07
AFM1	−0.473	±1.62	0
AFM2	−0.071	±1.95	0
AFM3	−0.326	±1.84	0
AFM4	−0.520	±2.01	0

amined the magnetic coupling among the Mn atoms, considering both collinear ferromagnetic and non-collinear configurations by incorporating the spin-orbit coupling (SOC) effect. Our results indicate that a non-collinear magnetic configuration is nearly close to, and slightly lower than, the collinear ferromagnetic configuration within the present computational setup. Total energy calculations over a range of lattice volumes demonstrate that the non-collinear phase is energetically stabilized by 29.55 meV/Mn, corresponding to an energy difference of 232.28 meV in a 2×1×1 supercell, relative to the collinear ferromagnetic state [see Figs. 3 (a)]. This energy difference suggests a preference for complex spin tilting over simple parallel alignment, as illustrated in Figs. 3 (b) and (c). Figures 3 (d) and (e) display the electronic structure and orbital-resolved density of states (PDOS) for Mn_2Ga_5. The total DOS at the Fermi level (E_F) is predominantly characterized by Mn-3d states, exhibiting a high degree of spin polarization, as evidenced by the significant splitting between the majority and minority spin channels. Within the itinerant electron framework, this electronic instability can be described by the Stoner model of ferromagnetism [18]. The high density of states $N(E_{\mathrm{F}})$ in the paramagnetic phase satisfies the Stoner criterion, $I \cdot N(E_{\mathrm{F}}) > 1$, where I is the Stoner exchange parameter, driving spontaneous spin splitting into an energetically favorable ferromagnetic ground state. The orbital-projected PDOS analysis reveals that the sharp peaks located between -4.0 eV and 0 eV are predominantly composed of Mn-3d sub-orbitals, including d_{z^2}, $d_{x^2-y^2}$, d_{xy}, and the degenerate d_{xz}/d_{yz} states. In contrast, the Ga-4p states are broadly distributed throughout the valence band, exhibiting strong covalent hybridization with the occupied Mn-3d states. While the majority-spin Mn-3d manifold is largely filled below E_{F}, the minority-spin states are shifted above the Fermi level (+0.2 eV to +2.0 eV), resulting in a robust local magnetic moment of $M_{\mathrm{Mn}} \approx 2.13$-$2.14$ μ_{B} [2]. Furthermore, the Ga atoms exhibit a small but distinct negative spin polariza-

tion ($-0.07\ \mu_B$), contributing an induced magnetic moment that is anti-aligned with the primary Mn moments (see Table II). This negative polarization is a characteristic feature of p-d covalent hybridization, where the itinerant Ga-4p electrons screen and mediate exchange coupling between the transition-metal centers. The MAE was evaluated by comparing the SOC-included total energies for different magnetization orientations. The calculated results show that the [100] and [110] directions within the ab-plane are nearly degenerate, with an energy difference of only $0.49\,\mu$eV/Mn, whereas the [001] direction exhibits higher energy. Figure 3 (f) shows the MAE as a function of the angle (θ) relative to the c-axis. The energy landscape depicts a pronounced anisotropy, with the minimum energy corresponding to spin orientations lying within the ab-plane. Conversely, the c-axis acts as the hard-axis, with an energy penalty of approximately 0.471 meV/Mn (3.768 meV per supercell) relative to the easy-plane orientation. Converted into volumetric units, this corresponds to an anisotropy constant of $K_u \approx 1442.1\,\mathrm{kJ/m^3}$, demonstrating substantial MAE in Mn_2Ga_5.

To further investigate the nature of phase transitions and dominant magnetic anisotropy in Mn_2Ga_5, we conducted isothermal magnetization measurements around T_C with the external magnetic field applied along the easy magnetization plane, as displayed in Fig. 4 (a). The Arrott plot of M^2 vs. H/M provides essential information about ferromagnetic transitions. Consequently, the data were transformed into an Arrott plot under the Landau mean-field theory framework ($\beta = 0.5$, $\gamma = 1.0$) [40], as illustrated in Fig. 4 (b). According to Banerjee's criterion, a positive slope in the high-field regime signifies a second-order phase transition, while a negative slope is characteristic of a first-order transition [41]. All isotherms in Fig. 4 (b) exhibit positive slopes, indicating a continuous second-order paramagnetic-to-ferromagnetic transition.

Within the Arrott plot framework, M^2 vs. H/M should manifest as parallel straight lines in the high-field regime, with the isotherm at T_C expected to pass through the origin. However, as depicted in Fig. 4 (b), these curves exhibit nonlinear and non-parallel trends in the high-field region. This deviation indicates that the Arrott plot constructed using the Landau mean-field model is insufficient for rigorously describing the critical behavior of Mn_2Ga_5. Instead, it necessitates the consideration of spin fluctuations and electronic correlations [42]. More generally, magnetic behaviors can be characterized by the Arrott-Noakes equation of state [21]:

$$(H/M)^{1/\gamma} = \frac{(T - T_C)}{T_C} + (M/M_1)^{1/\beta} \tag{1}$$

Here, M_1 is a constant, and β and γ denote the critical exponents, which can be deduced using the following functions [43, 44]:

$$M_S(T) = M_0(-\varepsilon)^{\beta}, \quad \varepsilon < 0, T < T_C \tag{2}$$

$$\chi_0^{-1}(T) = (h_0/M_0)\varepsilon^{\gamma}, \quad \varepsilon > 0, T > T_C \tag{3}$$

$$M = DH^{1/\delta}, \quad \varepsilon = 0, T = T_C \tag{4}$$

Here, $\varepsilon = (T - T_C)/T_C$ denotes the reduced temperature, while h_0/M_0 and D represent the critical amplitudes. The critical exponents (β, γ, and δ) are associated with the spontaneous magnetization (M_S) below T_C, initial susceptibility (χ_0^{-1}) above T_C, and the isothermal magnetization, respectively. Given the inadequacy of the conventional Arrott plot for Mn_2Ga_5, the Arrott-Noakes framework was employed to develop modified Arrott plots (MAPs) with $M^{1/\beta}$ vs. $(H/M)^{1/\gamma}$ [21]. These MAPs incorporate four theoretical models under the 3D structure, including the tricritical mean-field model ($\beta = 0.25$, $\gamma = 1.0$) [45], the 3D-Heisenberg model ($\beta = 0.365$, $\gamma = 1.386$), the 3D-Ising model ($\beta = 0.325$, $\gamma = 1.240$), and the 3D-XY model ($\beta = 0.346$, $\gamma = 1.316$) [42], as shown in Figs. 4 (c-f).

In the low-field regime, the replotted isotherms exhibit a slight curvature due to averaging over randomly oriented magnetic domains [44]. In the high-field region, all MAPs display quasi-linear behavior. To identify the optimal model for spin interactions and critical behavior in Mn_2Ga_5, we employ the normalized slopes (NS) method, defined as $S(T) = dM^{1/\beta}/d(H/M)^{1/\gamma}$. For an ideal MAP, the optimal model is characterized by examining whether all isotherms display consistent high-field slopes, resulting in an NS value close to 1. As illustrated in Fig. 5 (a), none of the canonical models considered reproduces the ideal $NS = 1$, indicating that the critical behavior of Mn_2Ga_5 cannot be assigned unambiguously to any of these conventional universality classes. Notably, among four theoretical models, the 3D-Ising model provides the best agreement with the data on both sides of the T_C with the smallest deviation from unity, whereas the 3D-XY and Heisenberg models show comparable behaviors. Trial analyses were performed using the exponent sets of all considered models. Among them the 3D-Ising exponents yield stable high-field intercepts for both $M_S(T)$ and $\chi_0^{-1}(T)$ and was consequently used to initialize the subsequent iterative analysis. A self-consistent iterative modified Arrott procedure was then employed to determine the critical exponents [46]. To minimize possible contributions from low-field domain effects and demagnetization effects, only the high-field linear regions of the isotherms were considered. All linear extrapolations were performed in the field range of 20-50 kOe. First, the intercepts of the linear high-field regions of the isotherms were extrapolated to obtain M_S and χ_0^{-1}, which were fitted using Eqs. (2) and (3), respectively. The extracted β and γ were subsequently used to construct new MAPs, with the procedure repeated until convergence, yielding stable and self-consistent MAP values. Consequently, the final temperature-dependent values of $M_S(T)$ and $\chi_0^{-1}(T)$ are shown in Fig. 5 (b), yielding $\beta = 0.303 \pm 0.003$ with $T_C = 446.62 \pm 0.03$ K and $\gamma = 1.181 \pm 0.006$ with $T_C = 447.07 \pm 0.08$ K. The

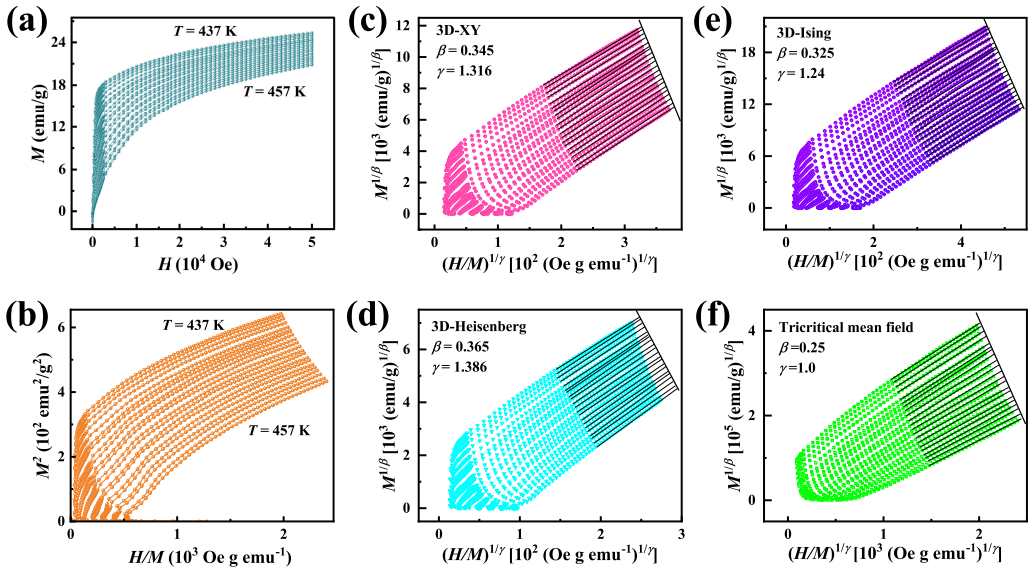


FIG. 4. (a) Initial isothermal magnetization curves along the easy plane from $T = 437$ K to $T = 457$ K. (b) Arrott plot of M^2 vs. H/M. Modified Arrott plots (MAPs) of $M^{1/\beta}$ vs. $(H/M)^{1/\gamma}$ for various theoretical models under the 3D frameworks: (c) 3D-XY model ($\beta = 0.345$, $\gamma = 1.316$), (d) 3D-Heisenberg model ($\beta = 0.365$, $\gamma = 1.386$), (e) 3D-Ising model ($\beta = 0.325$, $\gamma = 1.24$), and (f) tricritical mean-field model ($\beta = 0.25$, $\gamma = 1.0$).

normalized slopes, recalculated from the final iterative MAP, were also included in Fig. 5 (a), which remain close to unity in the vicinity of T_C, confirming the reliability of the extracted critical exponents.

To further verify the accuracy of the obtained critical values, we employ the Kouvel-Fisher (KF) technique [47, 48]:

$$\frac{M_S(T)}{d[M_S(T)]/dT} = \frac{T - T_C}{\beta} \tag{5}$$

$$\frac{\chi_0^{-1}(T)}{d[\chi_0^{-1}(T)]/dT} = \frac{T - T_C}{\gamma} \tag{6}$$

As shown in Fig. 5 (c), both $M_S(dM_S/dT)^{-1}$ vs. T and $\chi_0^{-1}(d\chi_0^{-1}/dT)^{-1}$ vs. T can be fitted using Eqs. (5) and (6). The slopes correspond to $1/\beta$ and $1/\gamma$, while the intercepts provide T_C. The KF analysis produces nearly identical values: $\beta = 0.301 \pm 0.006$ with $T_C = 446.67 \pm 0.07$ K and $\gamma = 1.163 \pm 0.002$ with $T_C = 447.13 \pm 0.08$ K. The agreement between the modified Arrott and KF methods confirms the self-consistency of the extracted effective exponents. Uncertainties were obtained from the fitting covariance, and the linear fits show good goodness-of-fit within the selected fitting windows.

The third critical exponent, δ, can be determined from the critical isotherm on a logarithmic scale. Figure 5 (d) displays the critical isotherm $M(H)$ at $T_C = 447$ K, with an inset illustrating the same data on a logarithmic scale. Fitting the curve to Eq. (4) yields $\delta = 4.875 \pm 0.002$. Alternatively, the Widom scaling relation can be employed to evaluate the critical exponents, relating β, γ, and δ as follows [49]:

$$\delta = 1 + \frac{\gamma}{\beta} \tag{7}$$

Using the β and γ values obtained from the MAP and KF plots, we estimate $\delta = 4.895 \pm 0.008$ and $\delta = 4.856 \pm 0.007$, respectively. These estimates align with the critical isotherm analysis, further confirming the reliability and accuracy of the determined critical exponents.

Figure 6 (a) presents the MAP constructed using the critical exponents $\beta = 0.303$ and $\gamma = 1.181$. The high-field regions of the isotherms are nearly linear and parallel, with all linear fits performed over the field range of 20-50 kOe. As expected at the critical temperature, the isotherm at $T_C = 447$ K approaches the origin. These features are consistent with the NS behavior of the final iterative MAP and support the self-consistency of the extracted critical parameters. It is important to ensure the self-consistency of the results and to check whether the derived critical exponents and T_C satisfy the scaling equation of state in the asymptotic critical region. According to the scaling hypothesis, the magnetic equation of state in this regime is given as [21]:

$$M(H, \varepsilon) = \varepsilon^{\beta} f_{\pm}(H/\varepsilon^{\beta+\gamma}) \tag{8}$$

The f_+ and f_- are regular functions, corresponding to $T > T_C$ and $T < T_C$, respectively. Equation (8) can also be simplified to:

$$m = f_{\pm}(h) \tag{9}$$

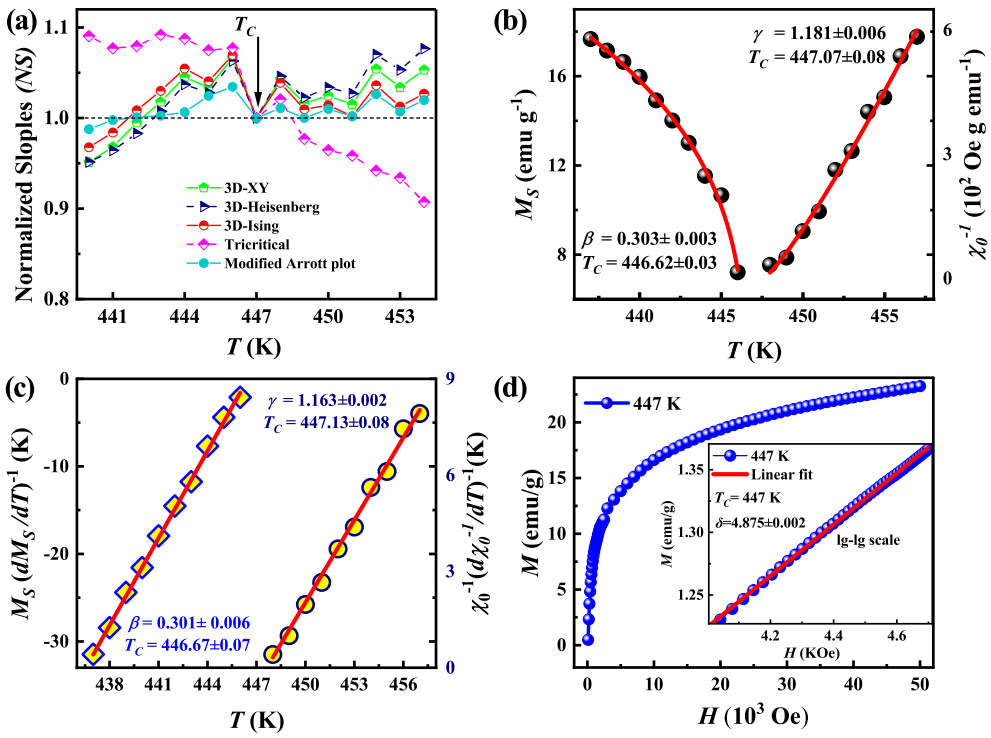


FIG. 5. (a) Normalized slopes $[NS = S(T)/S(T_C)]$ as a function of temperature for various theoretical models and the modified Arrott plot (MAP) obtained from the iterative analysis. (b) Temperature dependence of the spontaneous magnetization $M_S(T)$ (left) and the inverse initial susceptibility $\chi_0^{-1}(T)$ (right) for Mn_2Ga_5, with solid lines representing the fitting curves. (c) Kouvel-Fisher plots of $M_S(dM_S/dT)^{-1}$ (left) and $\chi_0^{-1}(d\chi_0^{-1}/dT)^{-1}$ (right) for Mn_2Ga_5, with the fitted curves providing estimates for the critical exponents. (d) Isothermal magnetization $M(H)$ at $T_C = 447$ K for Mn_2Ga_5. Inset: The same plot on a log-log scale with a solid fitting curve.

Here, $m \equiv \varepsilon^{-\beta} M(H, \epsilon)$ defines the normalized magnetization, and $h \equiv H\epsilon^{-(\beta+\gamma)}$ represents the normalized field. According to Eq. (8), the correct set of critical exponents should collapse the data into two independent curves corresponding to $T > T_C$ and $T < T_C$. As illustrated in Figure 6 (b), all isotherms merge into two distinct curves on either side of T_C. The plot of m^2 vs. h/m (Figure 6 (c) provides further evidence that the interactions are accurately renormalized in the critical regime, in agreement with the scaling equation of state.

The critical exponents for Mn_2Ga_5 extracted using various methods, along with those of different theoretical models, are summarized in Table III. The comparison indicates that Mn_2Ga_5 does not exactly follow any single canonical universality class [52–54]. Nevertheless, the extracted critical exponents are very close to those of the 3D-Ising model, suggesting an effective 3D-Ising-like critical regime with possible deviations induced by anisotropy-driven crossover effects. Overall, the extracted critical exponents are internally consistent across the MAP, KF, critical-isotherm, and scaling-collapse analyses. Previous investigations indicated that the critical exponent β for 2D-magnets should fall within the range of $0.1 \leq \beta \leq 0.25$ [55]. Interestingly, the value of β for Mn_2Ga_5 exceeds 0.25, clearly indicating a clear 3D characteristic, specifically with a spatial dimensionality $d = 3$. Notably, the extracted critical exponents do not precisely align with the theoretical values of the standard 3D-Ising model, which suggests deviations from an ideal single universality limit. This discrepancy suggests the presence of complex magnetic interactions in Mn_2Ga_5, which may arise from several factors, including dipole-dipole interactions [56], long-range Ruderman-Kittel-Kasuya-Yosida (RKKY) interactions [42], interactions extending beyond nearest neighbors [57], or significant MAE [41].

In a homogeneous magnet, the exchange interaction $J(r)$ determines the universality class of a phase transition. Therefore, it is essential to investigate the range of magnetic interactions in Mn_2Ga_5. The renormalization-group (RG) theory predicts that the exchange coupling decays as [55]:

$$J(r) \sim 1/r^{d+\sigma} \tag{10}$$

where σ is a positive constant and r represents the spatial

TABLE III. Comparison of critical exponents of Mn_2Ga_5 with different theoretical models and related materials. (MAP : modified Arrott plot; KFP : Kouvel-Fisher plot; CI : Critical isotherm).

Composition	Ref.	Technique	β	γ	δ	$J(r)$
Mn_2Ga_5	This work	MAP	0.303 ± 0.003	1.181 ± 0.006	4.895 ± 0.008	$r^{-4.91}$
Mn_2Ga_5	This work	KFP	0.301 ± 0.006	1.163 ± 0.002	4.856 ± 0.007	
Mn_2Ga_5	This work	CI			4.875 ± 0.002	
Mean field	[42]	Theory	0.5	1.0	3.0	
3D Heisenberg	[42]	Theory	0.365	1.386	4.80	
3D XY	[42]	Theory	0.345	1.316	4.81	
3D Ising	[42]	Theory	0.325	1.24	4.82	
Tricritical mean-field	[45]	Theory	0.25	1.0	5.0	
Fe_3GaTe_2	[50]	Theory	0.398(3)	1.102(14)	3.769(56)	$r^{-4.74}$
Cr_2Te_3	[51]	Theory	0.353(4)	1.213(5)	4.436(2)	$r^{-4.89}$
Mn_5Ge_3	[25]	Theory	0.336 ± 0.001	1.193 ± 0.03	4.61 ± 0.03	$r^{-4.855}$

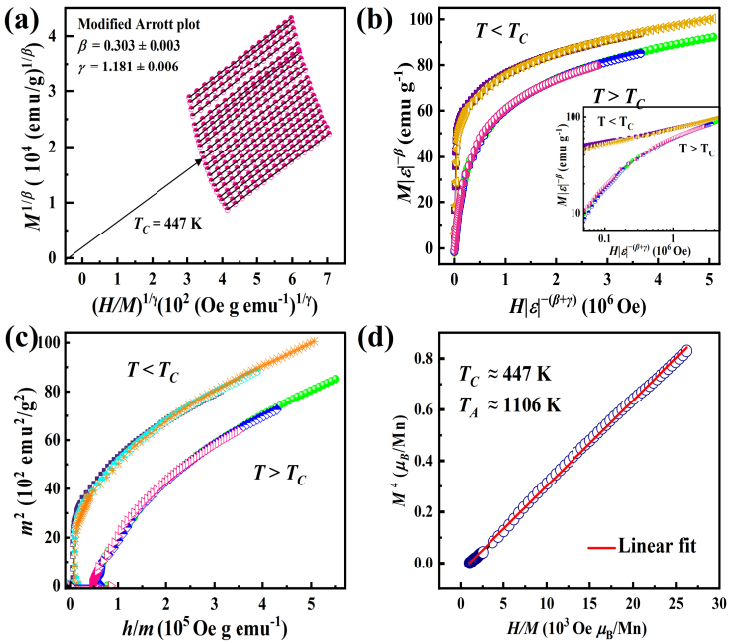


FIG. 6. (a) Modified Arrott plot constructed using the critical exponents $\beta = 0.303$ and $\gamma = 1.181$ for Mn_2Ga_5. (b) Scaling plots of renormalized magnetization m vs. renormalized field h for Mn_2Ga_5, both below and above $T_C = 447$ K. (c) m^2 vs. h/m plot for Mn_2Ga_5. (d) M^4 versus H/M plot at T_C using SCR theory.

distance. Within this theoretical framework, the susceptibility exponent γ can be expressed as:

$$\gamma \approx 1 + \frac{4}{d}\left(\frac{n+2}{n+8}\right)\Delta\sigma + \frac{8(n+2)(n-4)}{d^2(n+8)^2} \times \left[1 + \frac{2G(\frac{d}{2})(7n+20)}{(n-4)(n+8)}\right]\Delta\sigma^2 \quad (11)$$

where $\Delta\sigma = (\sigma - d/2)$, $G(d/2) = 3 - \frac{1}{4}(d/2)^2$, and n represents the spin dimensionality.

For 3D magnetic systems, $\sigma \geq 2$ corresponds to the short-range Heisenberg limit, where the interaction decays faster than r^{-5}. In contrast, $\sigma \leq 3/2$ corresponds to the long-range mean-field regime, where the interaction decreases more slowly than $r^{-4.5}$. Intermediate values of σ $(3/2 < \sigma < 2)$ represent effective long-range interaction regimes described by $J(r) \sim r^{-(d+\sigma)}$.

Following the procedure described in Ref. [58], the values of d, n, and σ were estimated by comparing the calculated γ with the experimentally obtained value. For different combinations of $\{d, n\}$, the parameter σ was varied in Eq. (11) until the calculated γ approached the experimental value of $\gamma = 1.181$. The remaining critical exponents, including ν, α, β, and δ, were calculated using the standard scaling relations [59]: $\nu = \gamma/\sigma$, $\alpha = 2 - \nu d$, $\beta = (2 - \alpha - \gamma)/2$, and $\delta = 1 + \gamma/\beta$. The analysis was repeated for various $\{d, n\}$ combinations, and the set $d = 3$, $n = 2$ with $\sigma = 1.91(3)$ was found to provide the closest

agreement with the experimentally obtained critical exponents $\beta = 0.367(2)$, $\gamma = 1.312(6)$, and $\delta = 4.574(3)$. Thus, in Mn_2Ga_5, the exchange interaction is estimated to decay approximately as $J(r) \sim r^{-4.91}$.

To quantitatively investigate the spin fluctuations in Mn_2Ga_5, we employ Takahashi's self-consistent renormalization (SCR) theory [60]. This theoretical framework explicitly accounts for the conservation of zero-point and thermal spin fluctuations, which are essential for understanding the physical properties of itinerant electron magnets near the T_C. According to SCR theory, at $T = T_C$, the magnetization (M) and the magnetic field (H) satisfy the following universal relation:

$$M^4 = \frac{1}{4.671}\left[\frac{T_C^2}{T_A^3}\right](H/M) \tag{12}$$

Here, T_A represents the dispersion of the spin fluctuation in wave-vector space, M is the magnetization in μ_B/Cr, and H is the magnetic field. Equation (12) predicts a linear relationship between M^4 and H/M at T_C, with the slope directly related to T_A. Figure 6 (d) presents the plot of M^4 and H/M for Mn_2Ga_5 at $T_C = 447$ K. The data were fitted to Eq. (12) using linear regression with the intercept fixed at zero, as required by Takahashi's theory. The fit exhibits excellent linearity, confirming the applicability of SCR to Mn_2Ga_5. Using the slopes obtained from the linear fit and $T_C = 447$ K, we computed the characteristic spin fluctuation parameter, $T_A = 1106$ K. Such linear behavior is characteristic of itinerant ferromagnets and has been observed in numerous systems such as $LaCo_2P_2$ [61], SmCoAsO [62], and many other itinerant systems. Within the SCR framework, the T_C can be further expressed in terms of the spontaneous magnetization (P_S) and two spin fluctuation parameters, T_A and T_0 as:

$$T_C = (60c)^{-3/4} P_S^{3/2} T_A^{3/4} T_0^{1/4} \tag{13}$$

Where $c = 0.3353$ is a constant, P_S is the spontaneous magnetization, and T_0 is the energy width of the dynamical spin fluctuation spectrum (in K). By using the values of T_C, P_S, and T_A, we obtained the parameter $T_0 = 3334$ K. In accordance with the SCR theory of spin fluctuations, the ratio T_C/T_0 serves as a key parameter characterizing the degree of itinerancy or localization of the spin moments. Materials with $T_C/T_0 \ll 1$ exhibit a pronounced itinerant character with well-developed spin fluctuations, while those with $T_C/T_0 \approx 1$ correspond to the localized moment limit. For Mn_2Ga_5, we obtain $T_C/T_0 = 0.134$, which is significantly lower than 1, suggesting the itinerant nature of Mn_2Ga_5.

For the itinerant magnet Mn_2Ga_5, the observed critical phenomenon stems from three microscopic factors. Firstly, its exceptional MAE strongly modifies the spin fluctuations and influences the effective order-parameter symmetry near T_C [7]. Secondly, the hybridization of Ga-4p and Mn-3d orbitals near the Fermi level not only mediates itinerant exchange but also introduces strong SOC and anisotropic hopping [2]. Thirdly, the identification of the ab-plane as the easy plane establishes a preferred in-plane magnetic orientation and modifies the symmetry of spin fluctuations, which may contribute to anisotropy-driven crossover effects between different universality regimes. Although the extracted critical exponents show similarity to the 3D-Ising model, the easy-plane magnetic anisotropy indicates that Mn_2Ga_5 cannot be classified as an ideal uniaxial Ising system. Instead, the observed critical behavior may represent an anisotropic 3D crossover regime involving Ising-XY like fluctuations. Similar anisotropy-influenced critical behavior has been reported in other itinerant ferromagnetic systems such as Fe_3GaTe_2, Cr_2Te_3, and Mn_5Ge_3 [50, 51, 63], where the interplay between electronic structure, magnetic anisotropy, and exchange interactions influences the critical behavior. For example, layered Fe_3GaTe_2 exhibits critical exponents ($\beta \approx 0.398$, $\gamma \approx 1.102$) attributed to its large perpendicular anisotropy (3.88×10^5 J/m^3, 9.5 nm, 300 K) [50][64]. Similarly, Cr_2Te_3 with $\beta = 0.353(4)$ and $\gamma = 1.213(5)$ is another itinerant ferromagnet with extremely large anisotropy ($K_u \sim 2065$ kJ/m^3). Mn_5Ge_3 ($\beta \approx 0.336$, $\gamma \approx 1.193$), an itinerant ferromagnet with non-collinear spin configurations, displays exponents that are closer to 3D-Ising-type universality [25]. This conclusion is further supported by comparison with $K_{0.79}Co_2S_2$, where the critical exponents were close to those of the 3D-Ising model despite the presence of easy-plane magnetic anisotropy, suggesting a complex relationship between anisotropy and universality class [65]. Thus, Mn_2Ga_5 presents a compelling case for unraveling the interplay between itinerant exchange, anisotropy, and universality in magnetic phase transitions, thereby validating RG predictions for anisotropy-controlled universality. This understanding is crucial for predicting critical behavior in correlated electron systems with competing interactions. Beyond Mn_2Ga_5, these results offer a framework for understanding how electronic structure and MAE determine universality classes in complex magnetic materials. These findings not only advance fundamental understanding but also hold significant implications for the development of high-temperature magnetic and spintronic applications.

IV. CONCLUSION

In summary, we conducted a comprehensive analysis of the critical behavior of itinerant Mn_2Ga_5 single crystal with an above-room-temperature T_C. Magnetization analysis revealed a second-order paramagnetic-to-ferromagnetic transition at $T_C \approx 447$ K. The critical exponents $\beta = 0.303$, $\gamma = 1.181$, and $\delta = 4.875$ were obtained using a series of techniques. These critical exponents adhere to Widom scaling, demonstrating the robustness and self-consistency of our analysis. The spin interaction in Mn_2Ga_5 decays as $J(r) \approx r^{-4.91}$. First-principles calculations using DFT reveal a ferromagnetic

ground state with a possible canted non-collinear magnetic configuration in Mn_2Ga_5. Since direct experimental evidence for this non-collinear spin arrangement is beyond the scope of the present work, further investigations using neutron diffraction or resonant magnetic x-ray scattering would be valuable for directly probing the microscopic spin configuration. A substantial MAE of $K_u = 1442.1$ kJ/m^3 was estimated. Furthermore, the self-consistent renormalization (SCR) theory identifies Mn_2Ga_5 as an in-plane itinerant ferromagnet. Our contribution resolves a fundamental question regarding the emergence of universality in anisotropic itinerant magnets. Overall, this study offers crucial insights and opens avenues for future exploration of Mn_2Ga_5 in high-temperature magnetic and spintronic applications.

ACKNOWLEDGMENTS

This work was supported by the National Key R&D Program of China (Grant No. 2024YFA1611103), the Strategic Priority Research Program (B) of the Chinese Academy of Sciences (CAS) (Grant No. XDB1720000), the National Natural Science Foundation of China (Grant Nos. 12374129, 12374128, and 22393913), the CAS Project for Young Scientists in Basic Research (Grant No. YSBR-084), the Anhui Provincial Major S&T Project (Grant No. s202305a12020005), the Anhui Provincial Natural Science Foundation (Grant Nos. 2408085J025, 2508085ZD013), and the Basic Research Program of the Chinese Academy of Sciences (CAS) Based on Major Scientific Infrastructures (Grant No. JZHKYPT-2021-08). Y.Z. acknowledges support from the China Postdoctoral Science Foundation (Grant No. 2024M753262) and Natural Science Foundation of Colleges and Universities in Anhui Province (Grant No. 2025AHGXZK40582). The first author acknowledges support from the ANSO-CAS-TWAS/UNESCO Scholarship for his ongoing PhD studies at the University of Science and Technology of China. This work was conducted as part of her doctoral research sponsored by the ANSO-CAS-TWAS/UNESCO Scholarship. We thank the Steady High Magnetic Field Facility (https://cstr.cn/31125.02.SHMFF.XRD) of CAS for data collection and analysis.

AUTHOR DECLARATIONS

Conflict of Interest−The authors have no conflict of interest to disclose.

Data Availability−The data that support the findings of this study are available from the corresponding authors upon reasonable request.

Author Contributions−Z.Q. initiated the project. S.Z., P.C., H.Z., X.X., Z.Q. synthesized and characterized the samples. S.Z., Y.Z., L.Z., Z.Q. performed magnetic measurements. M.G. performed HAADF-STEM measurements. M.I., Z.L. performed the first-principles calculations. S.Z., M.I., Y.Z., Z.L., L.Z., Z.Q. analyzed the data. All authors discussed the results and implications. S.Z., Y.Z., Z.L. drafted the manuscript with input from all authors. Z.Q., L.Z., and Z.L. supervised the project.

[1] I. Žutić, J. Fabian, and S. D. Sarma, Spintronics: Fundamentals and applications, Rev. Mod. Phys. **76**, 323 (2004).
[2] S.-H. Kim, M. Boström, and D.-K. Seo, Two-Dimensional Superdegeneracy and Structure-Magnetism Correlations in Strong Ferromagnet Mn_2Ga_5, J. Am. Chem. Soc. **130**, 13841 (2008).
[3] L. Hao and W. Xiong, An evaluation of the Mn–Ga system: Phase diagram, crystal structure, magnetism, and thermodynamic properties, Calphad **68**, 101722 (2020).
[4] K. Minakuchi, R. Y. Umetsu, K. Ishida, and R. Kainuma, Phase equilibria in the Mn-rich portion of Mn–Ga binary system, J. Alloys Compd. **537**, 332 (2012).
[5] M. Tillard and C. Belin, Investigation in the Ga-rich side of the Mn–Ga system: Synthesis and crystal structure of $MnGa_4$ and $MnGa_{5-x}$ ($x \sim 0.15$), Intermetallics **29**, 147 (2012).
[6] H. G. Meissner, K. Schubert, and T. R. Anantharaman, The constitution and structure of manganese-gallium alloys, Proc. Indian Acad. Sci. - Sect. A **61**, 340 (1965).
[7] W. Y. Zhang, P. Kharel, S. Valloppilly, R. Skomski, and D. J. Sellmyer, Synthesis and magnetism of single-phase Mn-Ga films, J. Appl. Phys. **117**, 17E306. (2015).
[8] F. Wu, S. Mizukami, D. Watanabe, H. Naganuma, M. Oogane, Y. Ando, and T. Miyazaki, Epitaxial $Mn_{2.5}Ga$ thin films with giant perpendicular magnetic anisotropy for spintronic devices, Appl. Phys. Lett. **94**, 122503 (2009).
[9] S. Mizukami, F. Wu, A. Sakuma, J. Walowski, D. Watanabe, T. Kubota, X. Zhang, H. Naganuma, M. Oogane, Y. Ando, and T. Miyazaki, Long-Lived Ultrafast Spin Precession in Manganese Alloys Films with a Large Perpendicular Magnetic Anisotropy, Phys. Rev. Lett. **106**, 117201 (2011).
[10] B. Balke, G. H. Fecher, J. Winterlik, and C. Felser, Mn_3Ga, a compensated ferrimagnet with high Curie temperature and low magnetic moment for spin torque transfer applications, Appl. Phys. Lett. **90**, 152504 (2007).
[11] J. M. D. Coey, New permanent magnets; manganese compounds, J. Phys. Condens. Matter **26**, 064211 (2014).
[12] L. Zhu, S. Nie, K. Meng, D. Pan, J. Zhao, and H. Zheng, Multifunctional $L1_0Mn_{1.5}Ga$ Films with Ultrahigh Coercivity, Giant Perpendicular Magnetocrystalline Anisotropy and Large Magnetic Energy Product, Adv. Mater. **24**, 4547 (2012).
[13] H. Kurt, K. Rode, M. Venkatesan, P. Stamenov, and J. M. D. Coey, $Mn_{3-x}Ga$ ($0 \leq x \leq 1$): Multifunctional thin film materials for spintronics and magnetic recording, Phys. Status Solidi B **248**, 2338 (2011).
[14] W. J. Kitchingman and P. L. Norman, Neutron diffrac-

tion, magnetic and superconducting measurements on vanadium–manganese–gallium alloys, J. Appl. Crystallogr **6**, 240 (1973).
[15] T. Matsui, M. Suzuki, K. Morii, and Y. Nakayama, Metastable ferromagnetic phase formation in 35–50 at. Mn-Ga thin films, J. Appl. Phys. **73**, 6683 (1993).
[16] G. Lamura, R. K. D. Tay, P. Gentile, C. Q. Xu, X. Ke, I. J. Onuorah, P. Bonfà, X. Xu, and T. Shiroka, Anisotropic superconductivity in the quasi-one-dimensional superconductor V_2Ga_5, J. Am. Chem. Soc. **130**, 1384 (2008).
[17] Y. Xu, X. Jin, J. Xiang, H. Zhang, and F. Tian, DFT + DMFT investigation of the magnetic phase transition in the itinerant ferromagnet Fe_3GaTe_2, Phys. Rev. B **111**, 155142 (2025).
[18] E. C. Stoner, Collective electron ferronmagnetism, Proc. A **165**, 372 (1938).
[19] J. Kübler, Theory of itinerant electron magnetism, Oxford University Press (2021).
[20] S. Yin, Jian, Shao-Kai, and H. Yao, Chiral tricritical point: A new universality class in dirac systems, Phys. Rev. Lett. **120**, 215702 (2018).
[21] A. Arrott and J. E. Noakes, Approximate Equation of State For Nickel Near its Critical Temperature, Phys. Rev. Lett. **19**, 786 (1967).
[22] M. Brando, D. Belitz, F. M. Grosche, and T. R. Kirkpatrick, Metallic quantum ferromagnets, Rev. Mod. Phys. **88**, 025006 (2016).
[23] M. Brando, D. Belitz, F. M. Grosche, and T. R. Kirkpatrick, Spin Fluctuations in Itinerant Electron Magnetism, Springer Nature Link .
[24] S. Swathi, K. Arun, U. D. Remya, A. Dzubinska, M. Reiffers, and R. Nagalakshmi, Ising critical behavior and room temperature magnetocaloric effect in itinerant ferromagnetic $Mn_5Ge_{2.9}Fe_{0.1}$ compound, Intermetallics **132**, 107164 (2021).
[25] J.-F. Lin, H. Wang, S. Xu, X.-Y. Wang, X.-Y. Zeng, Z.-Y. Dai, J. Gong, K. Han, Y.-T. Wang, X.-P. Ma, and T.-L. Xia, Critical behavior in the ferromagnet, EPL **146**, 16001 (2024).
[26] A. Pelissetto and E. V. A. Tripodo, Landau-Ginzburg-Wilson approach to critical phenomena in the presence of gauge symmetries, Phys. Rev. D **96**, 034505 (2017).
[27] M. Tachibana, Beginner's Guide to Flux Crystal Growth, Springer Japan, Tokyo (2017).
[28] G. Kresse and J. Furthmüller, Efficient iterative schemes for ab initio total-energy calculations using a plane-wave basis set, Phys. Rev. B **54**, 11169 (1996).
[29] P. E. Blöchl, Projector augmented-wave method, Phys. Rev. B **50**, 17953 (1994).
[30] H. J. Monkhorst and J. D. Pack, Special points for Brillouin-zone integrations, Phys. Rev. B **13**, 5188 (1976).
[31] Y. I. Dublenych, Ground States of the Ising Model on the Shastry-Sutherland Lattice and the Origin of the Fractional Magnetization Plateaus in Rare-Earth-Metal Tetraborides, Phys. Rev. Lett. **109**, 314 (2012).
[32] K. Siemensmeyer, E. Wulf, H.-J. Mikeska, K. Flachbart, S. Gabáni, S. Mat'aš, P. Priputen, A. Efdokimova, and N. Shitsevalova, Fractional Magnetization Plateaus and Magnetic Order in the Shastry-Sutherland Magnet TmB_4, Phys. Rev. Lett. **101**, 177201 (2008).
[33] See the Supplementary Material for the HAADF-STEM images, mapping of exchange interactions, angle-dependent magnetization measurement style, and calculation results..
[34] Y. Wang, J. Yan, J. Li, S. Wang, M. Song, J. Song, Z. Li, K. Chen, Y. Qin, L. Ling, *et al.*, Magnetic anisotropy and topological Hall effect in the trigonal chromium tellurides Cr_5Te_8, Phys. Rev. B **100**, 024434 (2019).
[35] A. Wang, A. Rahman, Z. Du, J. Zhao, F. Meng, W. Liu, J. Fan, C. Ma, M. Ge, L. Pi, L. Zhang, and Y. Zhang, Field-dependent anisotropic room-temperature ferromagnetism in Cr_3Te_4, Phys. Rev. Lett. **108**, 094429 (2023).
[36] M. Nandi, A. Thamizhavel, and S. K. Dhar, Anisotropic magnetic properties of trigonal $ErAl_2Ge_2$ single crystal, J. Phys.: Condens. Matter **32**, 185803 (2020).
[37] M. Matin, R. Mondal, A. Thamizhavel, A. Provino, P. Manfrinetti, and S. K. Dhar, Single crystal growth and anisotropic magnetic properties of $HoAl_2Ge_2$, AIP Adv. **8**, 055709 (2018).
[38] X. Yang, J. Pan, W. Gai, Y. Tao, H. Jia, L. Cao, and Y. Cao, Three-dimensional critical behavior and anisotropic magnetic entropy change in quasi-two-dimensional $LaCrSb_3$, Phys. Rev. B **105**, 024419 (2022).
[39] E. P. Wohlfarth, Magnetic properties of crystallineand amorphous alloys: A systematic discussion based on the Rhodes-Wohlfarth plot, J. Magn. Magn. Mater. **7**, 113 (1978).
[40] A. Arrott, Criterion for Ferromagnetism from Observations of Magnetic Isotherms, Phys. Rev. **108**, 1394 (1957).
[41] B. Banerjee, On a generalised approach to first and second order magnetic transitions, Phys. Lett. **12**, 16 (1964).
[42] S. N. Kaul, Static critical phenomena in ferromagnets with quenched disorder, J. Magn. Magn. Mater. **53**, 5 (1985).
[43] M. E. Fisher, The theory of equilibrium critical phenomena, Rep. Prog. Phys. **30**, 615 (1967).
[44] H. E. Stanley, *Introduction to Phase Transitions and Critical Phenomena* (Oxford University Press, London, 1971).
[45] D. Kim, B. Revaz, B. L. Zink, F. Hellman, J. J. Rhyne, and J. F. Mitchell, Tricritical Point and the Doping Dependence of the Order of the Ferromagnetic Phase Transition of $La_{1-x}Ca_xMnO_3$, Phys. Rev. Lett. **89**, 227202 (2022).
[46] A. K. Pramanik and A. Banerjee, Critical behavior at paramagnetic to ferromagnetic phase transition in $Pr_{0.5}Sr_{0.5}MnO_3$: A bulk magnetization study, Phys. Rev. B **79**, 214426 (2009).
[47] J. S. Kouvel and J. B. Comly, Magnetic Equation of State for Nickel Near Its Curie Point, Phys. Rev. Lett. **20**, 1237 (1968).
[48] M. E. Fisher, S.-k. Ma, and B. Nickel, Critical exponents for long-range interactions, Phys. Rev. Lett. **29**, 917 (1972).
[49] B. Widom, Equation of State in the Neighborhood of the Critical Point, J. Chem. Phys. **43**, 3898 (1965).
[50] Z. Chen, Y. Yang, T. Ying, and J. Guo, High-T_C Ferromagnetic Semiconductor in Thinned 3D Ising Ferromagnetic Metal Fe_3GaTe_2, Nano Lett. **24**, 993 (2024).
[51] S. Purwar, T. K. Bhowmik, S. Ghorai, and S. Thirupathaiah, 3D-Ising-type magnetic interactions stabilized by the extremely large uniaxial magnetocrystalline anisotropy in layered ferromagnetic Cr_2Te_3, Mater. To-

day Phys. **46**, 101522 (2024).
[52] B. Liu, Y. Zou, S. Zhou, L. Zhang, Z. Wang, H. Li, Z. Qu, and Y. Zhang, Critical behavior of the van der Waals bonded high T_C ferromagnet Fe_3GeTe_2, Sci. Rep. **7**, 6184 (2017).
[53] Y. Liu and C. Petrovic, Three-dimensional magnetic critical behavior in CrI_3, Phys. Rev. B **97**, 014420 (2018).
[54] L. Zhang, D. Menzel, C. Jin, H. Du, M. Ge, C. Zhang, L. Pi, M. Tian, and Y. Zhang, Critical behavior of the single-crystal helimagnet MnSi, Phys. Rev. B **91**, 024403 (2015).
[55] A. Taroni, S. T. Bramwell, and P. C. W. Holdsworth, Universal window for two-dimensional critical exponents, J. Phys. Condens. Matter **20**, 275233 (2008).
[56] N. Tateiwa, Y. Haga, T. D. Matsuda, E. Yamamoto, and Z. Fisk, Unconventional critical scaling of magnetization in ferromagnetic uranium superconductors UGe_2 and URhGe, Phys. Rev. B **89**, 064420 (2014).
[57] S. N. Kaul, Detailed magnetization study of an amorphous ferromagnet, Phys. Rev. B **24**, 6550 (1981).
[58] S. F. Fischer, S. N. Kaul, and H. Kronmüller, Critical magnetic properties of disordered polycrystalline $Cr_{75}Fe_{25}$ and $Cr_{70}Fe_{30}$ alloys, Phys. Rev. B **65**, 064443 (2002).
[59] J. K. Tiwari, H. C. Chauhan, and S. G. B. Kumar, 3D-Ising like ferromagnetism in skyrmionic-bubbles host infinite-layer $La_{0.825}Sr_{0.175}MnO_3$ manganite perovskite, J. Phys.: Condens. Matter **32**, 195803 (2020).
[60] Y. Takahashi, Spin Fluctuation Theory of Itinerant Electron Magnetism, Springer Berlin Heidelberg, Berlin, Heidelberg (2013).
[61] M. Imai, C. Michioka, H. Ueda, and K. Yoshimura, Static and dynamical magnetic properties of the itinerant ferromagnet $LaCo_2P_2$, Phys. Rev. B **99**, 184414 (2015).
[62] H. Ohta, C. Michioka, A. Matsuo, K. Kindo, and K. Yoshimura, Magnetic study of SmCoAsO showing a ferromagnetic-antiferromagnetic transition, Phys. Rev. B **82**, 054421 (2010).
[63] H. Liu, J. Fan, H. Zheng, J. Wang, C. Ma, H. Wang, L. Zhang, C. Wang, Y. Zhu, and H. Yang, Magnetic properties and critical behavior of quasi-2D layered Cr_4Te_5 thin film, Front. Phys. **18**, 13302 (2023).
[64] A. Rahman, M. U. Rehman, Z. Chen, W. Ahmad, Z. U. Rahman, Y. Yang, M. Ge, and L. Zhang, Multiple spin couplings and layer-valley interactions in room-temperature ferromagnetic Fe_3GaTe_2, Front. Phys. **20**, 033201 (2025).
[65] X. Chen, L. Duan, L. Liu, J. Zhao, G. Dai, W. Li, X. Wang, and C. Jin, Crystal growth, magnetic properties, and critical behavior of the itinerant ferromagnet $K_{0.79}Co_2S_2$, Phys. Rev. B **112**, 214402 (2025).